JOURNAL OF GEOPHYSICAL RESEARCH, VOL. 102, NO. B9, PAGES 20,395–20,411, SEPTEMBER 10, 1997

A strongly negative shear velocity gradient and lateral variability in the lowermost mantle beneath the Pacific

Jeroen Ritsema

Department of Geological Sciences, University of South Carolina, Columbia

Edward Garnero and Thorne Lay

Institute of Tectonics, University of California, Santa Cruz

Abstract. A new approach for constraining the seismic shear velocity structure above the core-mantle boundary is introduced, whereby SH-SKS differential travel times, amplitude ratios of SV/SKS, and $S_{\rm diff}$ waveshapes are simultaneously modeled. This procedure is applied to the lower mantle beneath the central Pacific using data from numerous deep-focus southwest Pacific earthquakes recorded in North America. We analyze 90 broadband and 248 digitized analog recordings for this source-receiver geometry. SH-SKS times are highly variable and up to 10 s larger than standard reference model predictions, indicating the presence of laterally varying low shear velocities in the study area. The travel times, however, do not constrain the depth extent or velocity gradient of the low-velocity region. SV/SKS amplitude ratios and SH waveforms are sensitive to the radial shear velocity profile, and when analyzed simultaneously with SH-SKS times, reveal up to 3% shear velocity reductions restricted to the lowermost 190±50 km of the mantle. Our preferred model for the central-eastern Pacific region (M1) has a strong negative gradient (with 0.5% reduction in velocity relative to the preliminary reference Earth model (PREM) at 2700 km depth and 3% reduction at 2891 km depth) and slight velocity reductions from 2000 to 2700 km depth (0–0.5% lower than PREM). Significant small-scale (100–500 km) shear velocity heterogeneity (0.5%–1%) is required to explain scatter in the differential times and amplitude ratios.

1. Introduction

Numerous seismological studies of the lower mantle have focused on the Pacific and surrounding regions mainly due to the dense path coverage provided by circum-Pacific seismic recordings of earthquakes in the southwest Pacific, northwest Pacific, and South America. Extensive research has led to maps of a shear velocity discontinuity about 250 km above the core-mantle boundary (CMB), anisotropic shear velocities within D", and ultralow P velocities at the base of the mantle. Furthermore, large-scale tomographic modeling has provided images of seismic velocity variations in D". These seismological models provide constraints on material properties and geodynamical processes operating at the core-mantle boundary (CMB) [see *Loper and Lay*, 1995, and references therein].

A pattern of predominantly higher-than-average seismic shear velocities beneath the circum-Pacific and lower-than-average shear velocities beneath the central Pacific has emerged. This is resolved both in whole-mantle aspherical models derived by tomographic inversions [e.g., *Dziewonski*, 1984; *Tanimoto*, 1990; *Su et al.*, 1994; *Masters et al.*, 1996; *Li and Romanowicz*, 1996] and in models of localized regions [e.g., *Lay and Helmberger*, 1983; *Garnero et al.*, 1988; *Wysession et al.*, 1995; *Sylvander and Souriau*, 1996]. This pattern is commonly attributed to hot, upwelling regions in the central Pacific and cold, downwelling regions along the Pacific margins associated with large-scale mantle circulation [see *Wysession*, 1996, for a recent discussion].

We present a new procedure for investigating both radial profiles and lateral variations of lower mantle shear velocity. This procedure relies on the properties of S waves that graze the CMB. It differs from previous techniques for measurement of the travel time [e.g., *Doornbos and Mondt*, 1979; *Wysession et al.*, 1992; *Valenzuela*, 1996] and (frequency dependent) amplitude decay [e.g., *Alexander and Phinney*, 1966; *Mula*, 1981; *Valenzuela*, 1996] of diffracted S in at least two aspects. First, we reference the travel time and amplitude of diffracting S waves to those of the SKS phase, sup-

Paper number 97JB01507.
0148-0227/97/97JB-01507$09.00

pressing the effects of upper mantle heterogeneities and source mislocation. Second, differential travel times and amplitude ratios of S and SKS phases are simultaneously modeled. In particular, we model overall trends in the distance dependence of the amplitudes and travel times, which constrains the seismic shear velocity gradient in D", and the radial extent of shear velocity perturbations from the D" region into the overlying mantle. The variations in observed times and amplitudes are used to estimate uncertainties in best-fitting one-dimensional (1-D) velocity profiles, and also to infer the presence of small scale (100–500 km) shear velocity variations. The S paths used are distributed over a relatively narrow geographical corridor with dense sampling of the lower mantle beneath the central-eastern Pacific ocean.

2. S and SKS: Travel Times and Amplitudes

Figure 1a shows path geometries of S and SKS waves (solid and dashed lines) for a 500-km-deep source and the preliminary reference Earth model (PREM) [*Dziewonski and Anderson*, 1981] velocity structure.

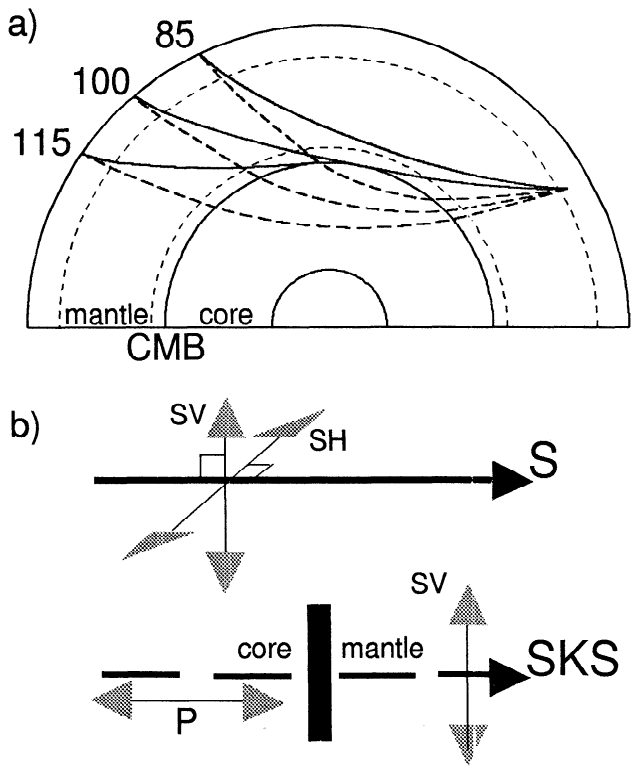

Figure 1. (a) Wave paths of S waves (solid) and SKS (dashed) computed for a 500-km-deep earthquake at distances of 85°, 100°, and 115° for the preliminary reference Earth model (PREM). The dotted lines are horizons at 670 km depth and 300 km above the core-mantle boundary (CMB). (b) Polarization directions (thin arrows) in relation to the propagation direction of S and SKS waves (bold solid and bold dashed arrows, respectively).

SKS propagates as a longitudinally polarized S wave through the mantle, converts to a P wave in the core, and reverts back to an SV wave for the final mantle segment. At distances beyond about 95°, S diffracts around the Earth's core and has a much longer path through D" than SKS. S waves involve both longitudinally polarized (SV) and horizontally polarized (SH) wave particle motion (see Figure 1b), which we distinguish by using the notation S^{SV} and S^{SH}, respectively.

Figure 2a displays a composite profile of radial component recordings of deep earthquakes in the Tonga-Fiji region. Broadband recordings from the Incorporated Research Institutions for Seismology (IRIS), Canadian National Seismic Network (CNSN), and United States National Seismic Network (USNSN), as well as digitized long-period World-Wide Standardized Seismic Network (WWSSN) data, are included in this figure. The second arrival is $SKKS$ (which has a path similar to SKS but with the addition of an underside reflection at the CMB), and the last arrival is S^{SV}. This profile exhibits two anomalous aspects of S propagation typical for many recordings for this path geometry and that are studied in this paper. First, S^{SV} is observed deep in the core shadow zone, indicating that these phases are not experiencing the strong amplitude reductions from diffraction that standard Earth models predict. Amplitudes of S^{SV} relative to SKS exceed predictions from PREM by a factor of 3 to 10. Second, S^{SV} arrives late with respect to SKS. Although S time delays relative to SKS are most accurately measured using the clearer S^{SH} component, S delays for this source-receiver geometry are also readily apparent in the late, large-amplitude S^{SV} arrivals in Figure 2a.

We analyze differential travel times of S^{SH} and SKS and amplitude ratios of S^{SV} and SKS for a total number of 338 (90 broadband recordings and 248 analog WWSSN) recordings from seismic stations in the United States and Canada at azimuths between 40° and 60° from southwest Pacific earthquakes (Table 1). Epicentral distances for these data range between 83° and 120°. Figure 2b displays the great-circles connecting events and stations (thin shaded lines) and surface projections of their S paths through D" beneath the central-eastern Pacific (bold lines). The sample region has dimensions of approximately 500×2000 km^2.

2.1. S^{SH}-SKS Differential Travel Times

Differential times between S^{SH} and SKS, denoted by $T_{S^{SH}-SKS}$, are primarily sensitive to shear velocity structure in the lower mantle. The effects of event mislocation and large-scale heterogeneous upper mantle structure are relatively small because S and SKS have very similar paths in the upper mantle. Anisotropic structure in the upper mantle may contribute several seconds to the scatter of $T_{S^{SH}-SKS}$; however, this signal has no systematic dependence with epicentral distance. In addition, contributions to the differential times from plausible aspherical outer-core structure are

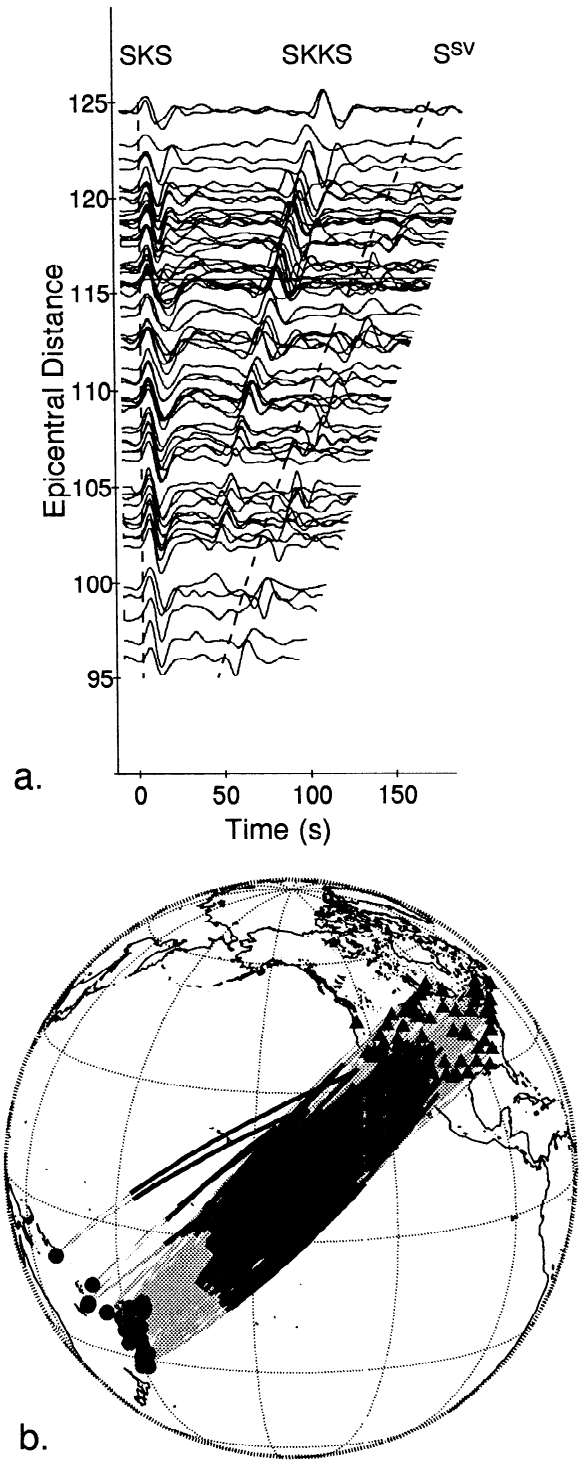

Figure 2. (a) Radial-component recordings of deep earthquakes in the Tonga-Fiji region from broadband and WWSSN seismic stations in North America. The recordings are offset by epicentral distance, normalized to have identical maximum trace amplitude, and aligned on SKS. The dotted lines indicate the relative arrival times of SKS and S^{SV}. (b) Great-circles connecting southwest Pacific earthquakes (circles) and seismic stations (triangles) in North America (thin shaded lines) and surface projections of arcs of S waves propagating in D" (bold lines) which outline the D" region studied.

negligible compared with those from the mantle as argued on dynamical [*Stevenson*, 1987] and seismological [*Garnero and Helmberger*, 1995b] grounds. Therefore $T_{S^{SH}-SKS}$ data are very useful for the study of lower mantle shear velocity structure and have been used in numerous studies [e.g., *Hales and Roberts*, 1971; *Garnero et al.*, 1988; *Young and Lay*, 1990; *Garnero and Helmberger*, 1993; *Liu and Dziewonski*, 1994; *Wysession et al.*, 1995; *Sylvander and Souriau*, 1996; *Kuo and Wu*, 1997].

$T_{S^{SH}-SKS}$ are measured from onsets of S^{SH} and SKS, picked on transverse and longitudinal component seismograms, respectively. For epicentral distances of 83^o to 120^o, SKS and S^{SH} are first arriving, high-amplitude shear waves on the radial and transverse components, respectively. Nearly all waveforms analyzed display clear onsets of SKS and S^{SH}. Picking onset times was preferred to picking peak amplitudes or use of waveform correlations, due to SKS waveform variations caused by anomalous SP_dKS interference [e.g., *Helmberger et al.*, 1996] and waveshape inconsistencies between predicted and observed S^{SH}. We omit recordings for which the differential onset times could not be measured with an accuracy of 1 s. The differential times, $T_{S^{SH}-SKS}$, were corrected to a source depth of 500 km and for effects of ellipticity using *Dziewonski and Gilbert* [1976], and were referenced to PREM predictions to obtain residual differential travel times:

$$\delta T_{S^{SH}-SKS} = [T_{S^{SH}-SKS}]^{\mathrm{OBS}} - [T_{S^{SH}-SKS}]^{\mathrm{PREM}}.$$

The residuals from broadband and WWSSN recordings, which show similar distribution with epicentral distance, are plotted in Figure 3a. The $\delta T_{S^{SH}-SKS}$ averages increase nearly linearly with distance to 9 s at a distance of 120^o. This general trend was also reported by *Garnero et al.* [1988], *Schweitzer* [1990], and *Tanaka and Hamaguchi* [1993].

2.2. S^{SV}/SKS Amplitude Ratios

S^{SV} waves are predicted to rapidly diminish in amplitude with distance into the core shadow zone, as most SV energy refracts to form seismic phases such as SKS, SKP, $SKKS$, and $SKKKS$, etc., and there is destructive interference with the oppositely polarized core-reflected ScS wave [*Chapman and Phinney*, 1972; *Choy*, 1977]. By referencing diffracted S^{SV} amplitudes to those of SKS (which usually have similar amplitude at the source), we obtain sensitivity to the shear velocity gradient above the CMB.

For 89 recordings containing a clear S^{SV} signal, the peak amplitudes of S^{SV} and SKS were used to construct the ratio $A_{S^{SV}/SKS}$. These amplitude ratios were referenced to those from synthetic seismograms generated by the reflectivity method [e.g., *Fuchs and Müller*,

Table 1. Event Parameters

Number	Date	Latitude °S	Longitude °E	Depth (km)	Strike	Dip	Rake	M_w[a]	Reference[b]
1	Sep. 10, 1962	21.1	179.2	640	147	43	226		R
2	July 4, 1963	26.3	-177.7	158					
3	Aug. 25, 1963	17.6	-178.7	557					
4	Aug. 5, 1964	32.2	179.8	210					
5	Dec. 28, 1964	22.1	-176.6	577	232	86	109		R
6	Apr. 10, 1965	17.8	-178.7	535					
7	Oct. 1, 1965	19.9	174.5	546					
8	March 17, 1966	21.1	-179.2	627	202	20	-101		R
9	Aug. 12, 1967	24.8	-177.4	144	268	73	100		R
10	Oct. 9, 1967	21.0	-179.2	605	54	86	-84		R
11	Nov. 4, 1968	14.2	172.0	585					
12	Jan. 24, 1969	21.9	-179.5	587	120	22	187		R
13	Feb. 10, 1969	22.8	178.8	635					
14	Apr. 20, 1970	18.8	169.3	243					
15	June 28, 1970	21.7	-179.4	587					
16	Nov. 20, 1971	23.5	-179.9	577					
17	March 30, 1972	25.7	179.6	479	181	80	60		R
18	May 22, 1972	17.8	-175.1	208					
19	Dec. 28, 1973	23.9	-180.0	517	178	71	70		R
20	March 23, 1974	23.9	-179.8	504	215	67	65		R
21	June 4, 1974	15.9	-175.0	256					
22	Oct. 21, 1974	18.0	-178.5	596					
23	Feb. 22, 1975	24.0	-178.9	333					
24	Aug. 5, 1979	22.7	-177.5	181	195	14	-112	6.5	CMT
25	July 20, 1980	17.9	-178.6	588	61	43	-173	6.3	CMT
26	April 28, 1981	23.7	-180.0	522	180	81	64	6.7	CMT
27	Sep. 28, 1981	29.3	-179.0	323	143	34	-164	6.5	CMT
28	Oct. 7, 1981	20.8	-178.6	620	289	30	-44	6.5	CMT
29	Jan. 26, 1983	30.4	-179.3	238	278	7	-78	7.0	CMT
30	June 1, 1983	17.0	-174.6	180	211	24	-97	6.5	CMT
31	April 25, 1984	17.3	-177.2	415	277	16	-4	6.3	CMT
32	June 15, 1984	15.8	-174.9	247	219	31	-57	6.6	CMT
33	Aug. 28, 1985	21.0	-179.0	625	210	23	-98	6.6	CMT
34	Oct. 6, 1985	18.9	169.4	256	178	68	51	6.1	CMT
35	May 26, 1985	20.1	178.7	553	197	21	-176	7.1	CMT
36	May 26, 1985	21.8	-179.1	583	312	64	-35	6.8	CMT
37	June 16, 1986	22.0	-178.8	547	241	19	-70	7.0	CMT
38	March 10, 1988	20.9	-178.7	623	334	33	-9	6.6	CMT
39	March 11, 1989	17.7	-174.5	246	128	23	18	6.9	CMT
40	June 8, 1990	18.7	-178.9	500	311	70	-61	6.4	CMT
41	June 23, 1990	21.6	-176.5	181	264	12	-26	6.8	CMT
42	June 26, 1990	22.0	-179.5	593	205	88	75	6.2	CMT
43	July 10, 1990	10.3	161.1	69	262	85	80	6.4	CMT
44	July 22, 1990	23.5	179.9	565	216	69	45	6.3	USGS
45	Sep. 30, 1991	21.0	-178.6	580	45	81	-96	6.9	CMT
46	Nov. 1, 1991	30.1	-178.0	48	202	30	99	6.6	CMT
47	Dec. 3, 1991	26.3	178.6	581	303	7	26	6.3	CMT
48	June 25, 1992	28.1	-176.7	18	232	23	130	6.5	CMT
49	July 11, 1992	22.3	-178.5	381	167	18	-131	7.2	CMT
50	Aug. 4, 1992	21.5	-177.9	278	108	56	-163	6.0	CMT
51	Aug. 30, 1992	17.7	-178.8	573	135	60	50	6.4	CMT
52	Oct. 11, 1992	19.3	168.9	157	185	78	123	7.4	CMT
53	Nov. 12, 1992	22.4	-178.1	368	211	14	-91	6.2	CMT
54	Dec. 12, 1992	32.0	-178.2	60	217	24	116	6.3	CMT
55	March 21, 1993	17.7	-178.8	590	66	41	-177	6.3	CMT
56	April 16, 1993	17.7	-178.9	568	8	88	-134	6.9	CMT
57	Aug. 7, 1993	23.9	179.8	580	98	29	-175	6.7	CMT
58	March 9, 1994	17.7	-178.6	570	18	65	-109	7.7	USGS
59	March 9, 1994	22.0	-179.6	590	17	87	-73	6.5	CMT

[a]from Harvard CMT.
[b]focal mechanism from R, *Richter* [1979]; CMT, Harvard CMT; USGS, U.S. Geological Survey MT solution.

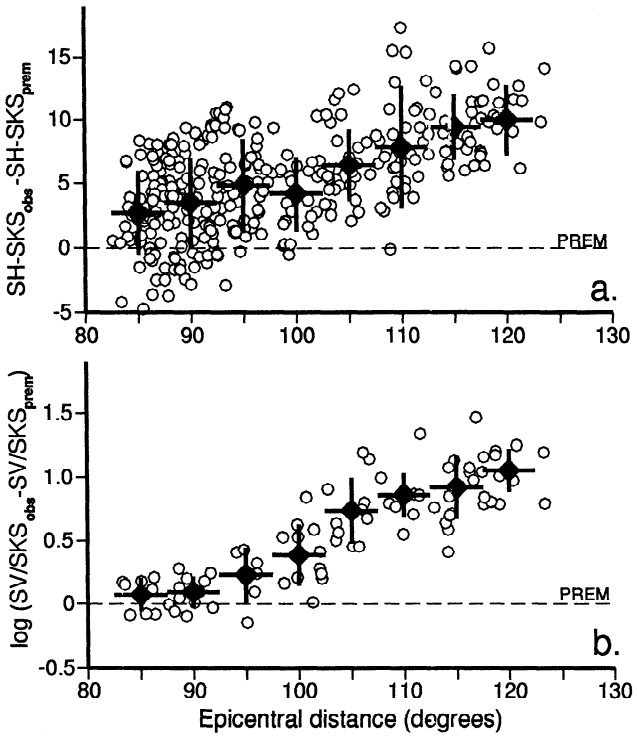

Figure 3. (a) Residual travel times $\delta T_{SSH-SKS}$ and (b) residual amplitude ratios $\delta A_{SSV/SKS}$ with respect to PREM predictions (dashed lines). Open and solid circles represent measurements made using long-period WWSSN and broadband seismic stations, respectively. Diamonds represent average values determined using the combined WWSSN and broadband data set. The horizontal bars indicate the 5° distance range over which the average value is determined, and the vertical bar indicates the standard error of average values.

1971] using source parameters in Table 1. This yields residual amplitude ratios

$$\log\left[\delta A_{SSV/SKS}\right] = \log\left[A_{SSV/SKS}\right]^{\mathrm{OBS}} - \log\left[A_{SSV/SKS}\right]^{\mathrm{PREM}}.$$

The distribution of $\log[\delta A_{SSV/SKS}]$ with epicentral distance is displayed in Figure 3b. As in Figure 3a, average values of residual amplitude ratios are determined over 5° distance intervals using the combined broadband and WWSSN data set. Data with S^{SV} amplitudes below noise level, which may include PREM-like S^{SV}/SKS ratios, are not included. This somewhat skews the data distribution toward anomalously large $\delta A_{SSV/SKS}$ values. In addition, poor rotations of the east–west and north–south components into radial and transverse components may be the cause of anomalous scatter of $\delta A_{SSV/SKS}$ values. This is especially a concern for poorly calibrated WWSSN recordings at the larger epicentral distances.

However, most recordings with excellent signal-to-noise ratios show a clearly observable S^{SV} signal. The $\log[\delta A_{SSV/SKS}]$ values increase systematically with increasing distance. At a distance of 120°, $\delta A_{SSV/SKS}$ is on average 10 times larger than predicted by PREM, reflecting the efficient S^{SV} propagation into the putative core shadow zone for this geometry, as shown in Figure 2a.

3. Simultaneous Modeling of S and SKS Differential Times and Amplitude Ratios

Large variations of $\delta T_{SSH-SKS}$ (up to 10 s) and $\delta A_{SSV/SKS}$ (up to a factor of 3) are readily observed in actual recordings and indicate that no 1-D model can account for all of our observations. However, without crossing paths it is impossible to derive reliable lateral variations of shear velocity causing the scatter in the distribution of $\delta T_{SSH-SKS}$ and $\delta A_{SSV/SKS}$. Clearly, the scatter is superimposed on a strong general trend that suggests a different background model than PREM. Thus we model the trends of the average $\delta T_{SSH-SKS}$ and $\log[\delta A_{SSV/SKS}]$ residuals with laterally homogeneous (1-D) shear velocity profiles to constrain gross features of the lower mantle shear velocity structure. A subsequent section discusses the implications of laterally heterogeneous shear velocity structure for our procedure.

3.1. Lower Mantle Shear Velocity Gradients

Figure 4 displays five groups of shear velocity profiles perturbed from PREM structure. Each group consists of three models which differ in their velocity reduction at the CMB. Groups L2000, L2400, L2600, L2700, and L2750 change linearly from depths of 2000, 2400, 2600, 2700, and 2750 km, respectively, to the CMB (2891 km depth), and have reductions from PREM at the CMB of 1%, 2%, or 3%. In the core and elsewhere in the mantle these models are identical to PREM. In the lower part of Figure 4, predictions of $\delta T_{SSH-SKS}$ (left column) and $\delta A_{SSV/SKS}$ (right column) for these models are compared with observations. The line styles used for the model predictions correspond to those used in plotting the velocity profiles. PREM predictions are the base lines ($\delta T_{SSH-SKS} = 0$; $\log[\delta A_{SSV/SKS}] = 0$).

The $\delta T_{SSH-SKS}$ predictions for different velocity reductions diverge beyond a critical epicentral distance, Δ_c. This distance is about 90° for group L2000 and increases to about 105° for group L2750. The $\delta T_{SSH-SKS}$ values are negative at distances smaller than 90°, due to a larger delay of SKS than S, since SKS propagates along a longer path than S through the zone of reduced shear velocities for these propagation distances. At distances larger than Δ_c, S diffracts around the core and $\delta T_{SSH-SKS}$ increases almost linearly with a gradient inversely proportional to shear velocity at the CMB. Our approach emphasizes modeling data for large distances (>100°) where S propagates through the D" region along a much longer path than SKS. One-

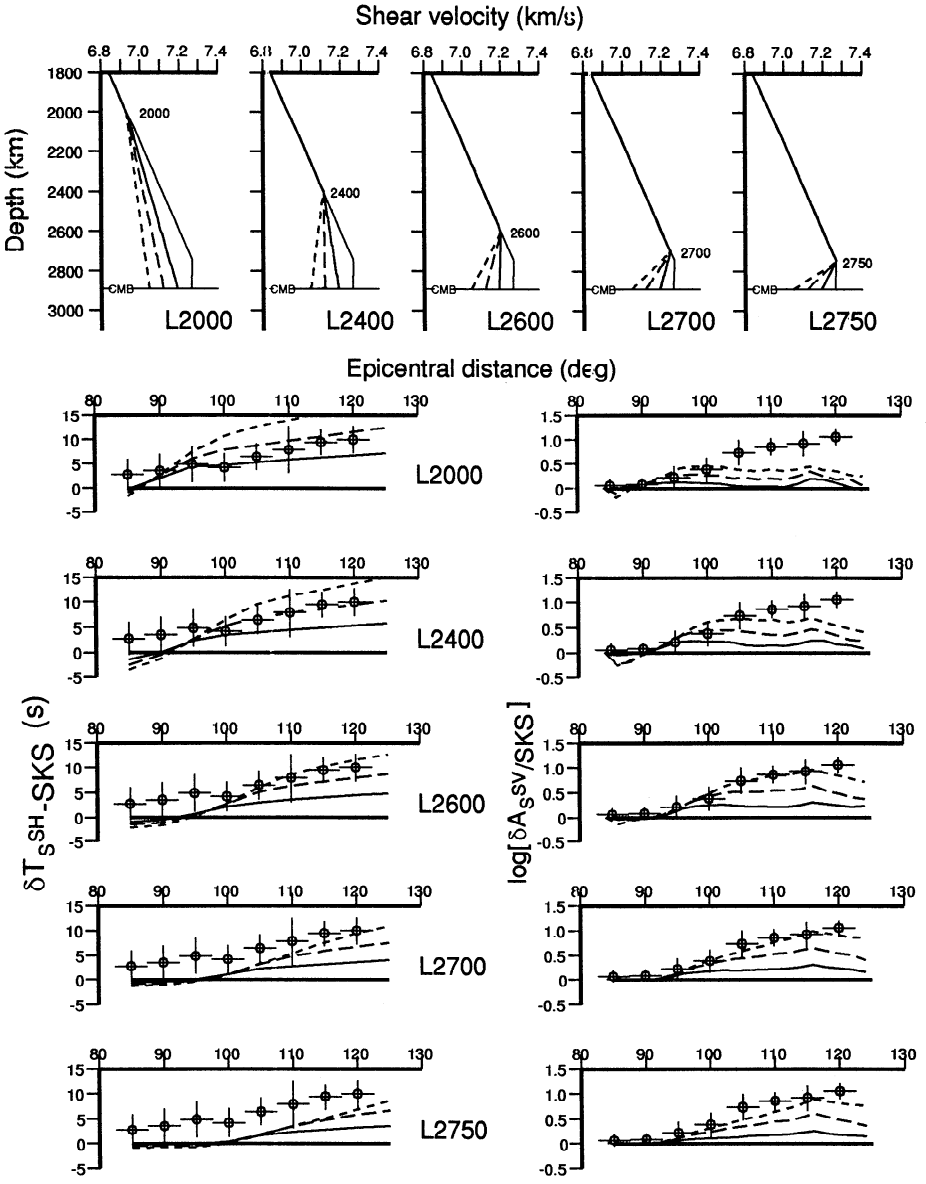

Figure 4. (top) Shear velocity model PREM (thin curve) and five groups of models with linear velocity profiles in the lowermost mantle. Shown are groups L2000, L2400, L2600, L2700, and L2750 which include constant-gradient velocity reductions with respect to the PREM below 2000, 2400, 2600, 2700, and 2750 km depth and which are identical to the PREM velocity structure elsewhere. Velocity reductions from PREM at the CMB of 1% (solid line), 2% (dashed line), and 3% (dotted line) are selected. (bottom) From top to bottom, $\delta T_{S^{SH}-SKS}$ (left column) and $\delta A_{S^{SV}/SKS}$ (right column) predicted for groups L2000–L2750 and 1–3% velocity reductions at the CMB are compared with residual averages of Figures 3a and 3b (circles and error bars). The line style used associates these predictions with the velocity profiles above. Residuals equal to zero (horizontal line) correspond to predictions for the global PREM shear velocity model. We use ray tracing to calculate $\delta T_{S^{SH}-SKS}$ and reflectivity seismograms to determine $\delta A_{S^{SV}/SKS}$ from S^{SV} and SKS peak amplitudes.

dimensional modeling of $\delta T_{S^{SH}-SKS}$ and $\delta A_{S^{SV}/SKS}$ is then most appropriate for the average structure along the S path in D". Heterogeneous structure which affects SKS alone is unlikely to account for the systematic trends in the data.

The $\delta T_{S^{SH}-SKS}$ is affected by the integrated shear velocity reduction in the lower mantle. Thus there is a strong trade-off between thickness of the zone of reduced velocities and the absolute velocity reduction at the CMB: A good match to $\delta T_{S^{SH}-SKS}$ for large epicentral distances is achieved for models L2000, L2400, and L2600, with velocity reductions at the CMB of 1%, 2%, and 3%, respectively. Models L2700 and L2750 fail to match observations for the range of reductions displayed.

Only models with strongly negative shear velocity

gradients match $\delta A_{S^{SV}/SKS}$. The model comparison in Figure 4 demonstrates that a low shear velocity region best reproducing both $\delta T_{S^{SH}-SKS}$ and $\delta A_{S^{SV}/SKS}$ must include a negative shear velocity gradient in the lowermost 200–300 km of the mantle (e.g., models L2600 and L2700) of about -0.07 to -0.10 km/s per 100 km, with CMB velocities about 3% lower than PREM. Models that can match $\delta T_{S^{SH}-SKS}$ with velocity reductions over depth ranges larger than 500 km (L2000 and L2400) and 1%–2% velocity reduction at the CMB, underestimate $\delta A_{S^{SV}/SKS}$. Models with low-velocity zones thinner than 150 km (e.g., L2750) and a 3% shear velocity reduction provide a good match to $\delta A_{S^{SV}/SKS}$ but significantly underestimate $\delta T_{S^{SH}-SKS}$.

3.2. The Radial Extent of Shear Velocity Reductions

Figure 5 compares fits to $\delta T_{S^{SH}-SKS}$ and $\delta A_{S^{SV}/SKS}$ for models that include shear velocity reductions that begin shallower in the mantle (2000 km depth) but retain deep mantle profiles similar to those of L2600 and L2700 of Figure 4. Figure 5 shows predictions from two-gradient models with 3% shear velocity reductions in D" initiating at depths 2600, 2650, 2700, and 2750

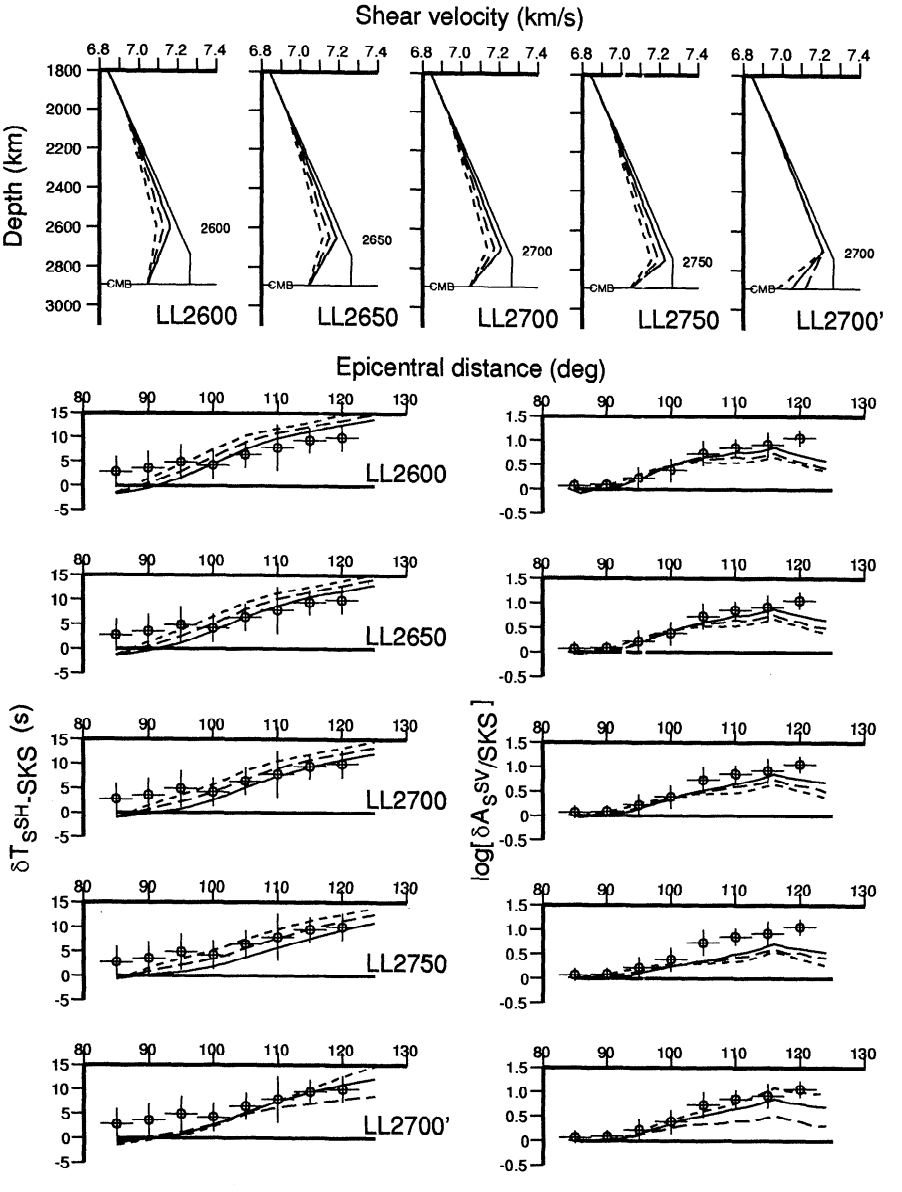

Figure 5. Comparison of average values of $\delta T_{S^{SH}-SKS}$ and $\delta A_{S^{SV}/SKS}$ measurements and predictions determined for model groups LL2000, LL2400, LL2600, LL2700, and LL2750 with shear velocity reductions at depths of 2600, 2650, 2700, and 2750 km, respectively of 0.5% (solid curve), 1% (dashed curve), and 1.5% (dotted curve) from PREM. The shear velocity reduction at the CMB is 3% for each model. In models of group LL2700', shear velocity at 2700 km depth is reduced by 0.5%, and velocity reductions at the CMB of 2% (solid curve), 3% (dashed curve), and 4% (dotted curve) are shown. The comparison of $\delta T_{S^{SH}-SKS}$ and $\delta A_{S^{SV}/SKS}$ predictions for these models is displayed in a fashion similar to Figure 4.

km (groups LL2600, LL2650, LL2700, and LL2750, respectively). Each group involves reductions of 0.5%, 1.0%, and 1.5% at the top of the D" zone. Also shown in the figure are models with variable reductions (2%, 3%, and 4%) over the bottom 190 km of the mantle (group LL2700') where the velocity at 2700 km is 0.5% less than in PREM. These models all yield $\delta T_{SSH-SKS}$ and $\delta A_{SSV/SKS}$ increases with increasing epicentral distance similar to the data averages. Upon closer inspection, however, it is apparent that only models from groups LL2650 and LL2700 with 0.5% reductions at the top of D" fit both the differential times and amplitudes over an extended distance range. A reference structure having 3% shear velocity reductions over the lowermost 190-240 km, with up to 0.5% reductions in the overlying 650-700 km, provides a good fit to our data averages. A slightly better fit to the $\delta T_{SSH-SKS}$ averages is achieved by LL2700, so we choose this structure as our preferred model. This structure, hereinafter referred to as M1, with a 0%–0.5% shear velocity reduction from 2000 to 2700 km depth, respectively, and a 0.5%–3.0% reduction from 2700 km depth to the CMB, respectively, has the basic features necessary to explain the monotonic increase of the time and amplitude residuals with epicentral distance. The negative shear velocity gradient in M1 is about -0.08 km/s per 100 km in the lowermost 190 km.

As Figure 5 demonstrates, we are able to constrain the depth of initiation of the zone of strong velocity reduction to about ±50 km. Given the scatter and uncertainties in $\delta T_{SSH-SKS}$ and $\delta A_{SSV/SKS}$ residuals and the anomalously large $\delta T_{SSH-SKS}$ observations between 85° and 95°, small modifications to M1 are permissible without significantly degrading the fit to the data. Thus a more detailed 1-D modeling effort with a wide range of parametrically more complex models is not useful for this data set, since the resolution is clearly limited. Nonetheless, we note that models with negative lowermost mantle gradients over wider depth intervals yield larger-than-observed time residuals, while reductions greater than 0.5% in the lower mantle above D" predict amplitude residuals smaller than observed.

We have also considered models that include a seismic velocity discontinuity at the top of D". Models having a first-order shear velocity increase smaller than 1–1.5% superimposed on a M1-type structure fit the data equally well. Larger magnitude increases, as well as discontinuity depths far above 200 km above the CMB, degrade the fit. While past evidence for a discontinuity in lower mantle shear structure beneath the Pacific exists [*Garnero et al.*, 1993; *Kendall and Shearer*, 1994; *Valenzuela*, 1996], the sensitivity of our data to details of such a structural feature is low.

Similarly, the presence of a variable thin layer (5-40 km) of ultralow-velocities proposed for the base of the mantle beneath the southwest Pacific [*Garnero and Helmberger*, 1995a; *Mori and Helmberger*, 1995; *Garnero and Helmberger*, 1996; J. Revenaugh and R. Meyers, Seismological mapping of the lowermost mantle: Further evidence of a possibly ubiquitous ultralow velocity zone, submitted to *Science*, 1997 (hereinafter referred to as submitted manuscript, 1997)] does not significantly affect the differential travel times or amplitude ratios. However, our 1-D model calculations indicate that a basal layer thicker than about 20 km can significantly alter diffracted wave shapes, incompatibly with our observations. Shear velocity reductions in the basal layer can be as large as 30% if partial melt is the cause [*Williams and Garnero*, 1996; J. Revenaugh and R. Meyers, submitted manuscript, 1997]. The thickness of the layer has been imaged as highly variable in the region of the southwest Pacific, possibly thinning to 5 km or less far from this region, and is mostly absent under the Americas (however, there are significant coverage limitations), which precludes us from properly addressing this issue in a 1-D modeling approach.

Our modeling effort thus focuses on the shear velocity gradient structure only, omitting possible contributions from a D" discontinuity or a low-velocity basal layer. Omission of these structural features does not alter our main conclusions concerning lower mantle gradients and depths of the large-scale velocity reductions. While there are key questions regarding a shear velocity discontinuity and ultralow-velocity basal layer in the highly variable central Pacific lower mantle, our data can place few constraints on these structures.

4. Analysis of Broadband S Waveforms

Model M1 reproduces trends in the $\delta T_{SSH-SKS}$ and $\delta A_{SSV/SKS}$ observations, particularly at distances beyond 100°, where S waves sample the lowermost mantle with longer path lengths. In this section, we further test this model by comparison of observed waveform recordings with synthetic seismograms.

4.1. Synthetic S^{SH} and S^{SV} waveforms for models PREM and M1

Two waveform characteristics are significantly different in reflectivity seismograms for PREM and model M1 (Figure 6). First, S^{SV} signals for model M1 have large amplitudes relative to SKS. For model PREM, the amplitude ratios $A_{SSV/SKS}$ at 108° and 116° are 20% and 8%, respectively, of the value at 95°. In contrast, $A_{SSV/SKS}$ ratios computed for M1 do not reduce as rapidly with increasing distance: At 108° and 116° $A_{SSV/SKS}$, ratios are 55% and 36%, respectively, of the value at 95°.

Second, S^{SH} waveforms for M1 are impulsive throughout the 95°–120° distance range. For model M1, even for a propagation distance of 110°, the geometrical S ray turns about 100 km above the CMB. Thus S waves encounter little distortion due to diffraction. For PREM, core diffraction causes S^{SH} waves to lose high-frequency energy and to broaden with increasing distance beyond the core's shadow [*Chapman and Phinney*, 1972].

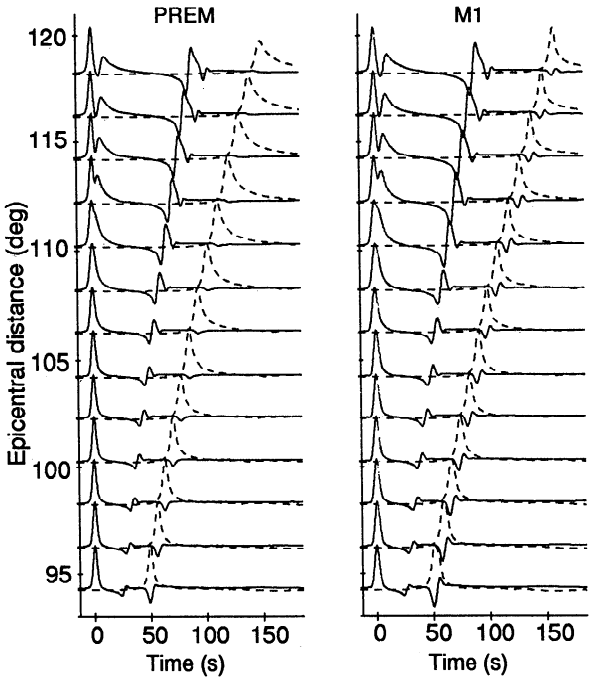

Figure 6. Time-distance profiles of radial (solid lines) and transverse (dashed lines) component displacement seismograms computed for a 500-km-deep earthquake and the shear velocity models PREM and M1. Seismograms are aligned on SKS and normalized by the SKS amplitude. Note the absence of S^{SV} arrivals and S^{SH} waveform broadening due to core diffraction at large distances for PREM.

4.2. S^{SV} and S^{SH} Observations

High-quality, digital, broadband waveforms from IRIS, USNSN, and CNSN stations in North America provide excellent S^{SH} and S^{SV} signals for comparison with PREM and M1 synthetics. Longitudinal component displacement recordings of events in Table 1 at broadband station HRV are shown in Figure 7. These events are at epicentral distances larger than 114°. Waveforms computed for models M1 and PREM are also shown.

Note that the S^{SV} amplitudes for nearly all recordings are much larger than predicted by PREM. This is also observed in recordings from other broadband and WWSSN stations not shown in this figure, and similar observations were reported by *Vinnik et al.* [1995] and *Garnero and Helmberger* [1995a]. For events 900608, 900626, 930321, 930807, and 940331 the S^{SV} amplitudes and waveforms are well reproduced by M1. S^{SV} is not observed above the noise level for events 900722 and 940316. However, due to the fault plane orientation, low-amplitude S^{SV} waves are predicted for model M1 (and PREM). Such recordings with unfavorable S^{SV} and SKS excitation are not included in the data collection of Figure 3b.

Despite the overall large amplitudes, S^{SV} signals exhibit considerable waveform and amplitude variability. This suggests that the shear velocity structure in the lower mantle has strong variability relative to a reference model like M1. For example, opposite SKS and S^{SV} first-motion polarities, predicted by M1, are not observed for colocated events 900626 and 940331. Very small amplitude S^{SV} is observed for event 940309, even though M1 synthetics suggest that an arrival should be observable well above the noise level. Anomalous S^{SV} waveshapes are present for events 900722 (double pulsed arrival) and 910930 (longer-period energy), although overall low signal levels may be responsible for these anomalous recordings.

Broadband recordings, and PREM and M1 synthetics of events 940309 and 940331 at stations across North America are shown in Figures 8 and 9, respectively. Several of these stations are located within 5° azimuth sectors of Tonga-Fiji earthquake epicenters and span a distance range of 30°. These profiles illustrate the decay of single-event S^{SV} and S^{SH} amplitudes with epicentral distance. As in Figure 7, S^{SV} amplitudes are well explained by M1 but also display quite variable behavior. The amplitude of S^{SV} decreases abruptly from station LSCT to stations LBNH and HRV, spanning just over 1° in epicentral distance range. The observed S^{SH} amplitudes are underpredicted by M1, possibly due to a focal mechanism change during rupture [*Goes and Ritsema*, 1995], but the sharpness of the S^{SH} waveform is well reproduced by M1 synthetics.

The broadband recordings of events 940331 (Figure 9), low-pass filtered for periods T > 5 s, also show large S^{SV} amplitudes similar to those in the M1 synthetics. S^{SV} amplitude and waveform variability are also present in the data. Large-amplitude S^{SV} at stations GAC, LSCT, and HRV are in contrast to the much smaller S^{SV} at LBNH, despite their proximity. As for event 940309, however, the pronounced narrow S^{SH} waveforms even at large distances are well reproduced by M1 but not by PREM.

5. Large- and Small-Scale Heterogeneity

The scatter in $\delta A_{SSV/SKS}$ and $\delta T_{SSH-SKS}$ indicates strong shear velocity fluctuations in our study region. The variation in $\delta A_{SSV/SKS}$ residuals has been discussed in the previous section. In this section we present examples of differences in time residuals clearly observable in recordings for event/station pairs with proximate lower mantle paths. By assuming that $\delta T_{SSH-SKS}$ variations are caused by shear velocity structure in D", we estimate the magnitude and scale length of shear velocity heterogeneity in D".

Figure 10a displays observations and PREM synthetics for event 921231 at five stations in California. These stations are within 2° epicentral distance and 9° azimuth range from the epicenter. Thus lower mantle S paths associated with these recordings are separated by less than 500 km. The SKS onsets are aligned, and identical time shifts are applied to the recorded and synthetic transverse component waveforms. The numbers plotted above the transverse component waveforms denote the difference in time of S^{SH} onsets of the synthetic and recorded waveforms ($T_{SSH-SKS}$). A varia-

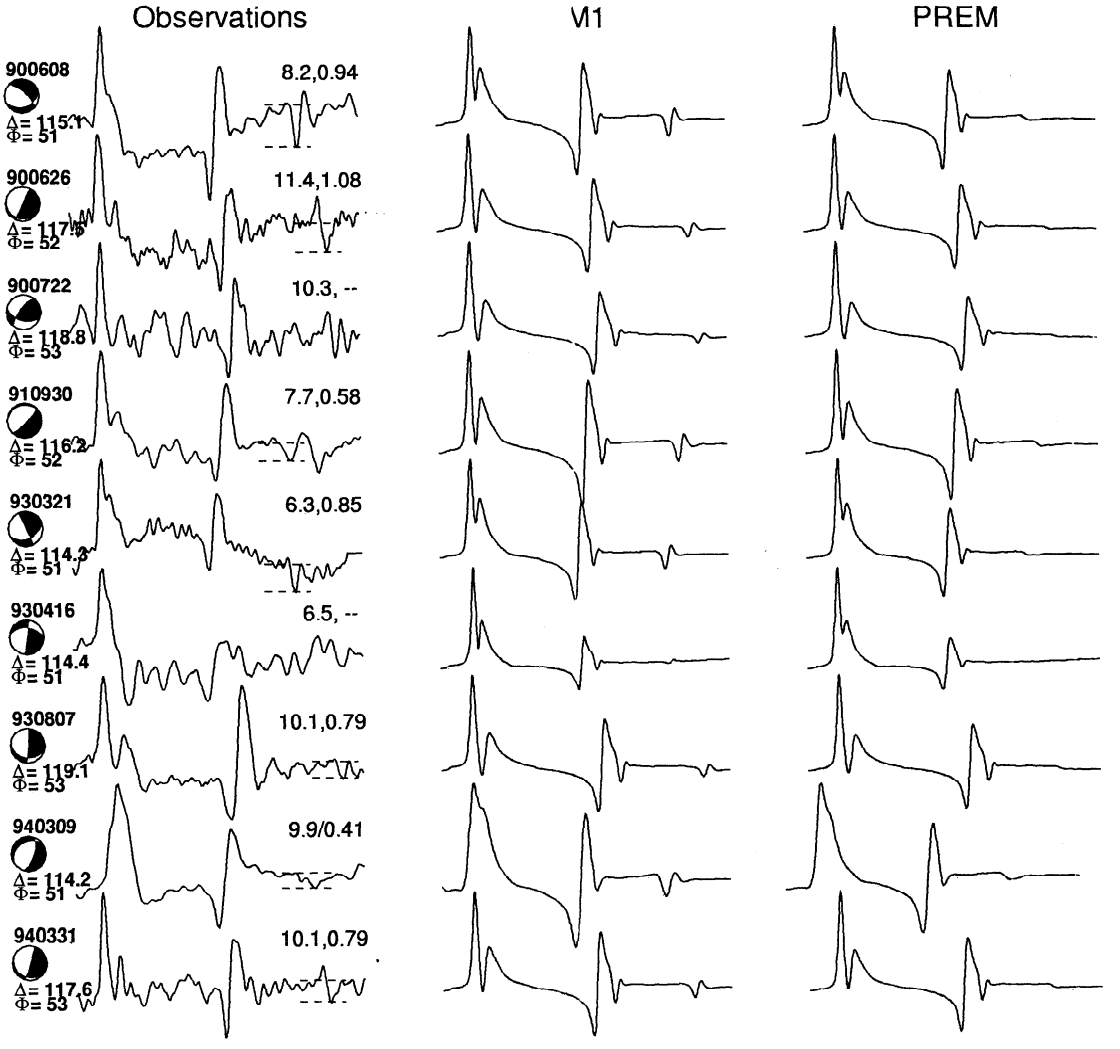

Figure 7. Comparison of radial component seismograms at station HRV (Harvard, Cambridge, Massachusetts) between observed SKS and S^{SV} and synthetic displacement seismograms, computed for models PREM and M1. Waveforms are normalized by maximum trace amplitude and have a duration of 200 s. Synthetic seismograms are computed using the reflectivity method and Harvard CMT source parameters, except for events 900722 and 940309, for which we used the USGS-MT moment tensor parameters. On the left of the waveform recordings, the focal mechanism, epicentral distance (Δ), and source azimuth (Φ) to station HRV are given. On the upper right of each recording, the $\delta T_{S^{SH}-SKS}$ and $\delta A_{S^{SV}/SKS}$ time and amplitude residuals, separated by a comma, are denoted. S^{SV} amplitudes are indicated by the horizontal bars at the S^{SV} arrivals. For recordings 900722 and 930416 the S^{SV} amplitude measurement is not made because of low signal quality.

tion of $T_{S^{SH}-SKS}$ of 4 s is evident in the recordings from station BAR in southern California to stations CMB and WDC in northern California. A similar comparison is made in Figure 10b. This figure compares recordings of events 920830 and 900623 at station CCM and recordings of 920804 and 921112 at HRV at distances near 99° and 116°.

Figure 10 indicates that significant heterogeneity exists for length scales less than 500 km in the narrow corridor from Fiji-Tonga to North America, giving rise to several seconds of variability in S delays. Also visible in the figure (particularly Figure 10a) are records possessing arrival times of S^{SV} later than S^{SH}. This phenomena of shear wave splitting of diffracted waves has been previously noted for this source-receiver geometry [*Vinnik et al.*, 1989, 1995] and attributed to anisotropy in the D" region [*Maupin*, 1994; *Vinnik et al.*, 1995]. In our approach, $T_{S^{SH}-SKS}$ is most sensitive to structure encountered by S^{SH}, i.e., V_{SH}. $A_{S^{SV}/SKS}$, on the other hand, is most sensitive to gradients in velocity structure traversed by S^{SV}, or V_{SV}. A small reduction in V_{SV} in relation to V_{SH} in the D" layer can explain the observed splits in our data. Since only a small portion of our data set has nonzero S^{SV}-S^{SH} times (which display significant variability), we again do not seek to explain this lower mantle feature in our 1-D modeling effort.

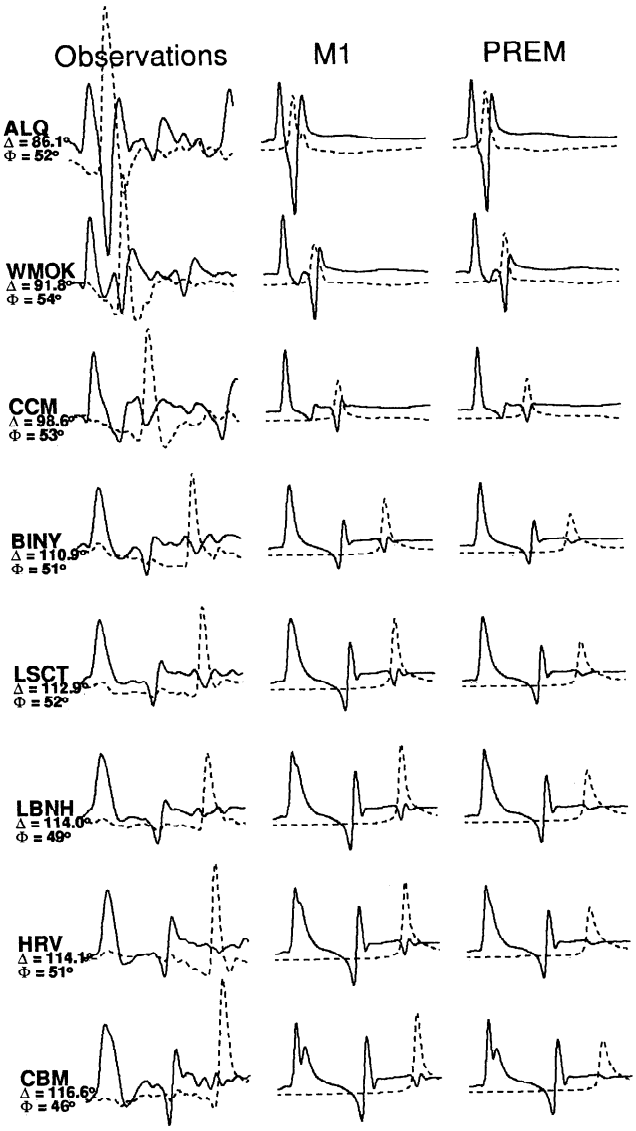

Figure 8. Comparison of observed (left) and synthetic displacement seismograms of event 940309, computed for models M1 (center) and PREM (right). The waveforms are normalized by the maximum trace amplitude and have a 200-s duration. Solid lines and dashed lines are the radial and transverse component recordings, respectively. Synthetic seismograms are computed using the reflectivity method and the USGS moment tensor parameters. Station name, epicentral distance (Δ), and source azimuth (Φ) are given on the left of the observed waveforms.

We note, however, that the degree of fit of predicted $\delta A_{S^{SV}/SKS}$ ratios to observations does not degrade for a model with an offset D" gradient (i.e., retaining the same D" gradient, but lowering absolute V_{SV} velocities by around 1%).

Since variations in $T_{S^{SH}-SKS}$ are observed for waveform recordings in the entire 100°–120° distance range (see Figure 3a), we assume that shear velocity variations are present in the entire depth range of D". For each path of Figure 2b, and for other paths in the Pacific, the average shear velocity perturbation in D" is estimated by dividing the path length of S in D" by the $\delta T_{S^{SH}-SKS}$ time associated with that path. The D" thickness is chosen to be 300 km. A different choice of D" thickness somewhat alters the magnitude of the resulting shear velocity perturbations in D" but not the pattern. We include only measurements for source–receiver distances larger than 100° to ensure long S paths in D" relative to SKS. Figures 11a–11g display the S paths in D" associated with the calculated shear wave perturbations (δV_S) in increments of 0.5%.

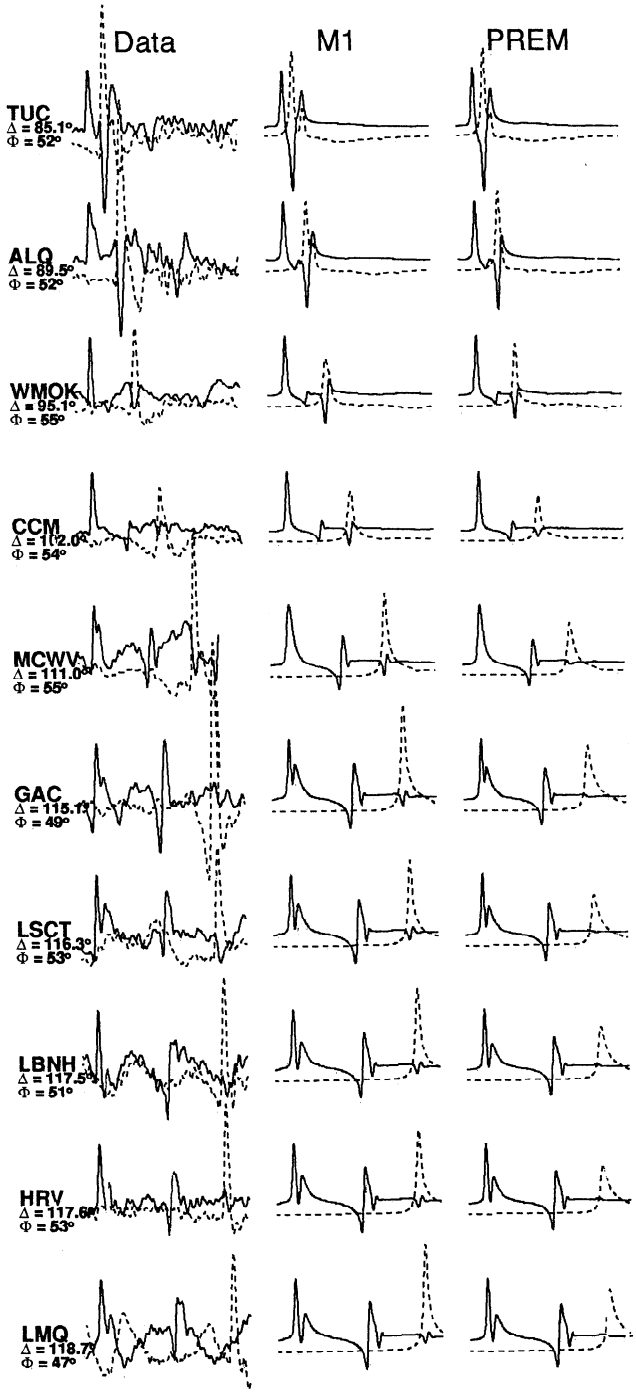

Figure 9. As in Figure 8 but for event 940331.

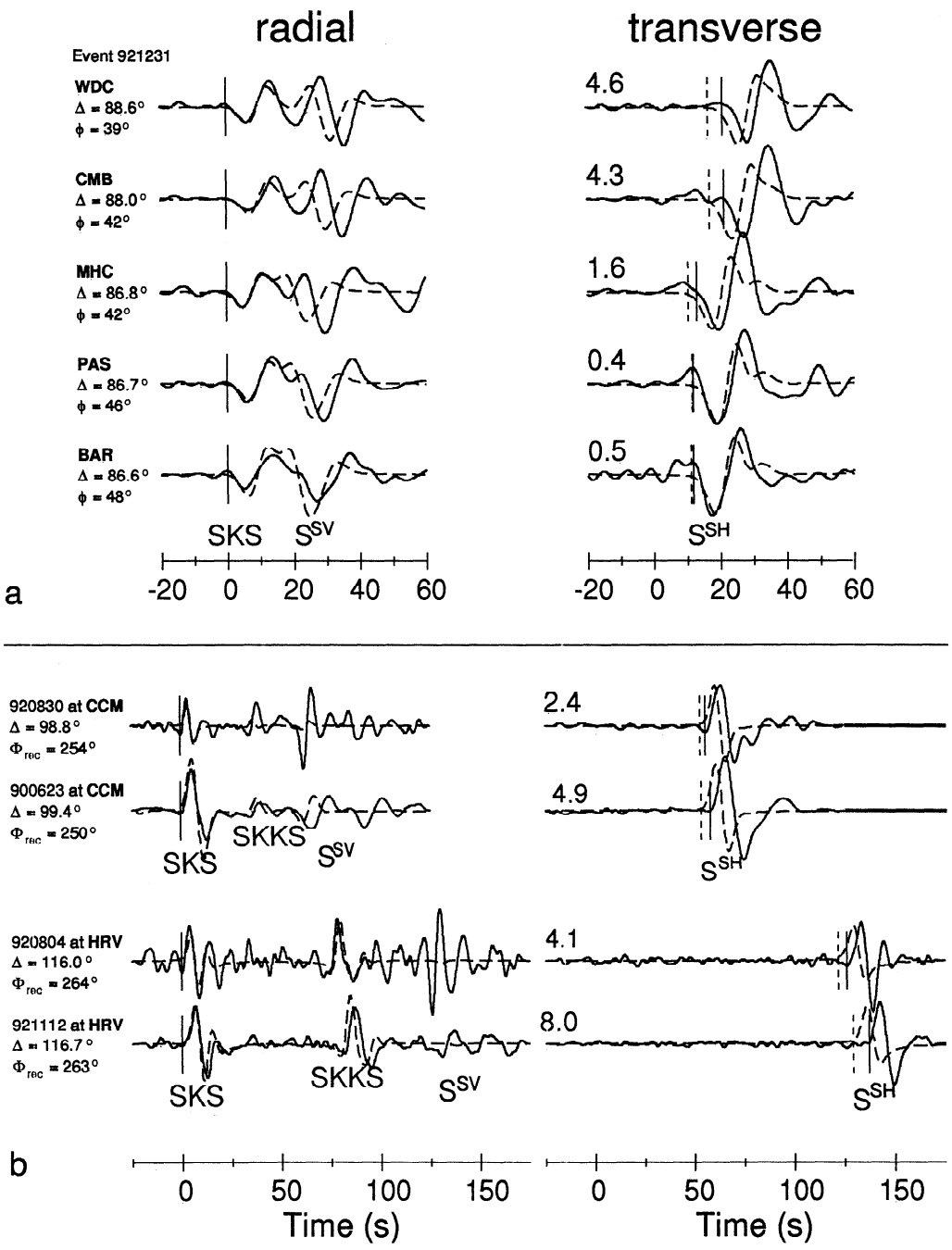

Figure 10. (a) Observed (solid lines) and synthetic (dashed lines) radial (left column) and transverse (right column) component seismograms of event 921231 from stations in California. Station names, epicentral distance (Δ), and station azimuth with respect to the event (Φ) are given on the left. All recordings are aligned on the SKS phase. Synthetics are computed using the PREM model. The onset times of S^{SH} for the observed and synthetic seismograms are indicated by solid and dashed vertical bars for the observed and synthetic waveforms, respectively. The number denoted above the transverse recordings is the difference in seconds of these time picks and represent $T_{S^{SH}-SKS}$ for these source receiver pairs. (b) Comparison between recordings of events 920830 and 900623 at station CCM (top) and between recordings of event 920804 and 921112 at station HRV (bottom). See Figure 10a for further details.

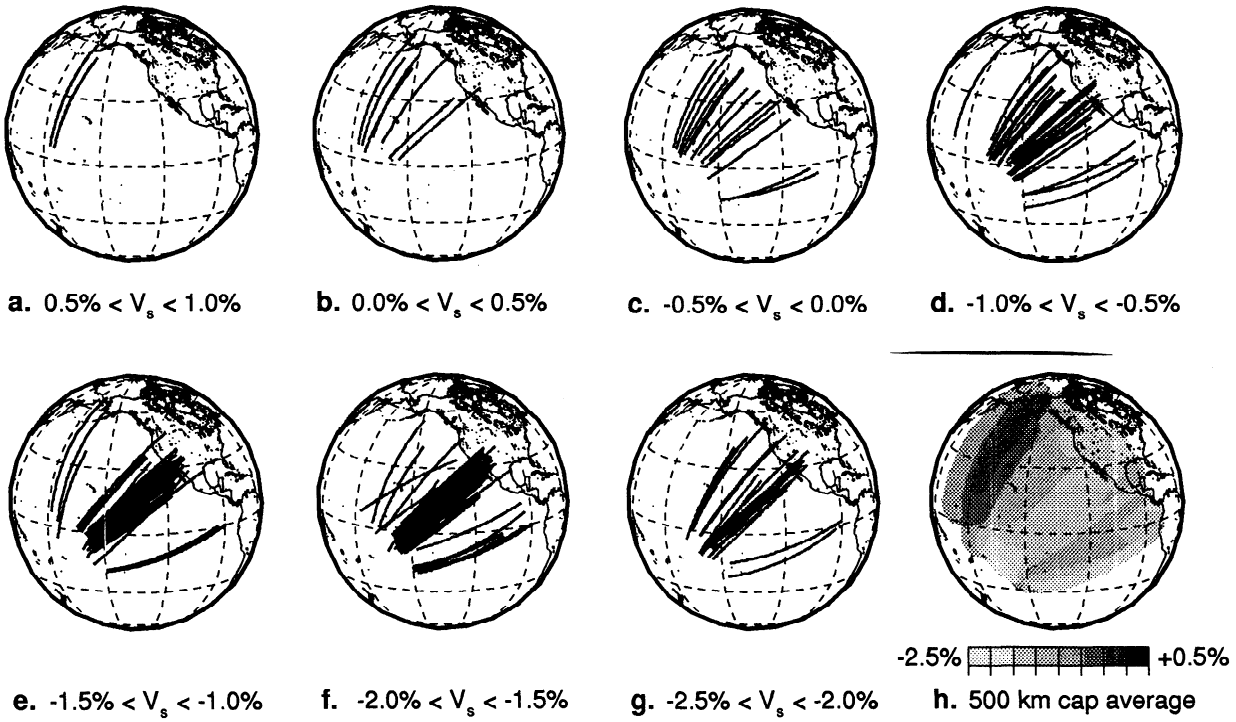

Figure 11. S paths in D" for which δT_{SSH_SKS} residual times imply shear velocity perturbations from PREM between (a) 0.5% < V_S < 1.0%, (b) 0.0% < V_S < 0.5%, (c) -0.5% < V_S < 0.0%, (d) -1.0% < V_S < -0.5%, (e) -1.5% < V_S < -1.0%, (f) -2.0% < V_S < -1.5%, (g) -2.5% < V_S < -2.0%. In Figure 11h shear velocity perturbations from PREM at locations in the Pacific region is are determined by averaging the seismic velocity perturbations of paths that traverse these locations within 500 km. This yields essentially a low-pass filtered (>500 km) display of the velocity perturbations for paths in Figures 11a–11g.

Short scale-length heterogeneity is strongly suggested due to the overlap of S paths requiring different velocity perturbations. This is particularly obvious for the abundance of paths in the central and northeastern Pacific used to derive M1. The average shear velocity reduction in M1 with respect to PREM in D" is about 1.5%. A number of paths (Figure 11c through 11g) suggest 0.5%–1% small-scale D" shear velocity variations about the M1 reference structure.

Large-scale shear velocity variations are also evident in Figure 11. Paths through the northern Pacific indicate primarily positive velocity perturbations, whereas large shear velocity reductions are associated only with northeastern and eastern Pacific paths. Figure 11h further emphasizes this by displaying a map of the shear velocity perturbations smoothed with a Gaussian cap average of 500 km radius. The elongated shape of shear velocity structure parallel to the S path in D" is due to lack of crossing ray path coverage, but the progressive decrease of shear velocity in D" from the northern Pacific to the eastern Pacific is required by the data. This has previously been reported by *Garnero et al.* [1993] and *Valenzuela* [1996].

6. Effects of Aspherical Mantle Structure on T_{SSH_SKS}

Without crossing ray path coverage, we are unable to image three-dimensional lateral variations in D" structure. Nonetheless, by referencing the travel times and amplitudes of S to those of SKS (thus suppressing contribution from upper mantle heterogeneities), and modeling the average trends in these times and amplitudes, we have imaged a 1-D reference structure appropriate for the lower mantle beneath the Pacific. However, S and SKS paths diverge strongly in the lower mantle even well above D". For example, at a distance of 120°, downgoing S and SKS paths are laterally separated by around 900 km at a depth of 2000 km.

Recent models of aspherical mantle structure have indicated large shear velocity anomalies in the lower mantle beneath the Pacific [e.g., *Su et al.*, 1994; *Masters et al.*, 1996]. Here we briefly explore the behavior of δT_{SSH_SKS} in the data with predictions of model M1, as well as predictions of an aspherical whole-mantle model. We choose the three-dimensional shear structure SKS12_WM13 (abbreviated SKS12 from here on) of *Liu and Dziewonski* [1994]. This model was chosen since it includes T_{SSH_SKS} data in its inversion. *Garnero and Helmberger* [1993] discuss the match to T_{SSH_SKS} times for earlier aspherical models for this geometry.

Figure 12a displays a cross section of SKS12 that intersects this study's source-receiver great-circle distribution (Figure 2b). Also shown are S and SKS wave geometries for epicentral distances of 85° and 120°. The white box indicates the lower mantle region traversed

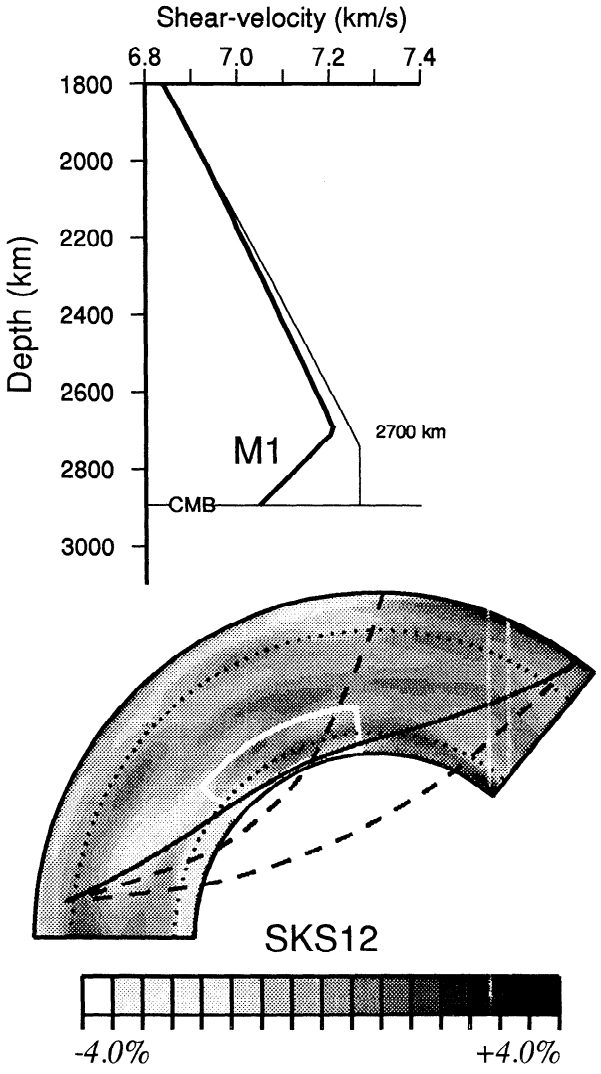

Figure 12. (bottom) Mantle cross section intersecting the Tonga-Fiji source region and the receiver region in North America, and the shear velocity perturbations from PREM of SKS12 (shaded region). The bold lines are wave paths of S at 85° and 120°, and the dashed lines are SKS paths at these distances. The white box outlines the lower mantle region appropriate for M1. The dotted lines represent the upper boundary of D" (300 km above the CMB) and the lower boundary of the upper mantle (660 km below the surface). (top) Shear velocity models PREM (thin line) and M1 (bold line).

by S waves for propagation distances larger than 100°, for which the M1 shear velocity structure is applicable. A low-velocity feature in SKS12 extends from the CMB into the midmantle near the source-region (white shading), which is one of the most pronounced lower mantle low-velocity features of that model. For both distances (85° and 120°), S traverses this structure with longer paths than SKS. This results in a positive $\delta T_{SSH-SKS}$ anomaly, which qualitatively agrees with the observations.

Figure 13 compares $\delta T_{SSH-SKS}$ predictions for models M1 (bold line) and SKS12 (open circles) with the observed values (solid triangles) from Figure 3b. Predictions for SKS12 are computed by ray-tracing the 1-D geometric ray path of each source-receiver pair through the aspherical structure (as done by *Garnero and Helmberger*, [1993]). Predictions from model M1 overlay observations over the whole distance range, while underpredicting the mean of the times at distances less than 100° (as discussed earlier). Model SKS12 underpredicts $\delta T_{SSH-SKS}$ for distances greater than 100° but has a mean at lower ranges closer to that of the observations than predicted by M1. For example, at distances less than 90°, SKS12 averages near 5 s for $\delta T_{SSH-SKS}$, while M1 predictions are less than zero (-1 to 0 s). The data averages for 85° and 90° are 2.5 and 3.5 s, respectively, which are closer to the SKS12 predictions.

Neither M1 nor any other 1-D velocity profile we tested produced the large $\delta T_{SSH-SKS}$ anomalies at the close-in distances. A 1-D model can reproduce this behavior only if significant midmantle velocity reductions are invoked, which results in a misfit of $\delta A_{SSV/SKS}$. Thus, as SKS12 demonstrates, lateral heterogeneities are necessary to reproduce such a feature. Preferential delays of the downgoing S (relative to SKS) in the midmantle and lower mantle beneath the source region (as depicted by SKS12, white shading, Figure 12) may contribute significantly to the large observed $\delta T_{SSH-SKS}$ anomalies between 83° and 100°. This anomaly can bias the $\delta T_{SSH-SKS}$ times (an increase) by up to 2 s. Not accounting for such structure can result in mapping midmantle anomalies into D". In this study, some of the larger distance data may thus have some contribution to the $\delta T_{SSH-SKS}$ anomalies from the midmantle beneath the source region. However, the present effort has focused on trends in the data beyond 100°, where $\delta T_{SSH-SKS}$ anomalies are as large as 10 s. A bias in some of our data will not alter our conclusions, and even subtracting 2 s from all of our $\delta T_{SSH-SKS}$ measurements still results in a shear velocity profile with a strongly negative gradient in the lowermost 200 km or so of the mantle, as in M1, but slightly less negative.

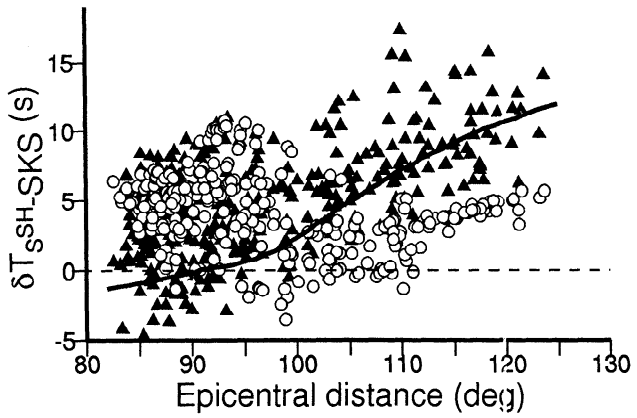

Figure 13. Comparison of $\delta T_{SSH-SKS}$ (solid triangles) with predictions for models SKS12 (open circles), M1 (solid line), and PREM (dashed line).

With resolution slowly improving in tomographic efforts, future work will entail correcting differential times for upper mantle and midmantle heterogeneity.

7. Discussion

Large estimated temperature contrasts across the CMB require the presence of a significant thermal boundary layer in D" [e.g., *Jeanloz*, 1990]. It is commonly assumed that the generally low velocity gradients in many seismic models are a result of this boundary layer. Using the PREM model, *Stacey and Loper* [1983] estimate the temperature increase across D" to be about 840 K. *Doornbos et al.* [1986] noted the substantial uncertainties in such estimates resulting from possible chemical inhomogeneity and seismic anisotropy in D".

Associating the strong negative shear velocity gradient of M1 with a thermal boundary layer in D" implies a temperature increase in D" much larger than 840 K, using the assumptions of *Stacey and Loper* [1983]. However, *Stacey and Loper* [1983] derive the temperature increase in D" on the basis of reduced velocity gradients for both P and S. *Young and Lay* [1989] conclude from an analysis of short-period P wave amplitude decay that the P wave gradient in D" is positive in this region. From the analysis of $P_{\rm diff}$ travel times, *Wysession et al.* [1992] also estimate average P velocity in D" to be slightly larger than in PREM. This suggests that the P and S wave structure may be very different. While more work needs to be done on the P wave structure, differing S and P velocity perturbations, together with the short-scale shear velocity variations (indicated by the strong scatter of $\delta T_{S^{SH}-SKS}$ and $\delta A_{S^{SV}/SKS}$), are not easily explained by strong thermal variations alone. This suggests the presence of compositional heterogeneity.

M1 suggests a rather small shear velocity reduction from PREM at depths between 2000 and 2700 km. The white box in Figure 12a indicates the lower mantle region traversed by S waves for which model M1 is most representative. In this region we resolve significant lower-than-PREM shear velocities in the lowermost 190±50 km of the mantle, consistent with the study of *Valenzuela* [1996] but in contrast to the average or faster-than-average velocities of model SKS12. Our study supports but does not constrain the presence of the midmantle low-velocity structure beneath the source region in model SKS12. However, the structure of M1 represents a limit to the radial extent of pronounced low velocities into the midmantle in the northeastern portion of our study area.

While we have set aside the issue of anisotropy in D", which will not affect our basic conclusions, we have instead developed an isotropic reference structure that accounts for the overall increase of differential travel times and amplitude ratios. This is essential, for it is very difficult to make reliable interpretations of S^{SV} signals at large distances into the core shadow zone without first understanding the basic background structure, which, of course, relates to fundamental issues such as whether these phases are truly diffracted or not. As we have shown, the introduction of strong negative gradients at the base of the mantle can cause significant S^{SV} amplitudes that might be misinterpreted as the result of anisotropy that converts S^{SH} energy into S^{SV}. Any attempt to interpret those signals should include the isotropic effects of strongly negative gradients. Some work along these lines has been presented by *Vinnik et al.* [1995].

8. Conclusions

A total of 338 $T_{S^{SH}-SKS}$ difference times and 89 $A_{S^{SV}/SKS}$ amplitude ratios determined from broadband and WWSSN recordings of Tonga-Fiji earthquakes at stations in North America have larger values than predicted by standard global seismological models such as PREM. These observations indicate low shear velocities in D" beneath the central and northeastern Pacific. A new approach is employed in which time and amplitude residuals are simultaneously analyzed. This provides strong constraints on the radial velocity structure that cannot be obtained when diffracted wave travel times alone are analyzed.

Forward modeling of residual averages as a function of epicentral distance with simple shear velocity profiles yields the best matching 1-D structure. Our favored model M1 has the following robust characteristics that apply to the lower mantle beneath the Pacific: (1) The shear velocity decreases between around 2700 (±50) km depth and the CMB with a gradient of -0.08 ± 0.03 km/s per 100 km. (2) The shear velocity in the lowermost 190 (± 50km) km of the mantle averages about 1.5% smaller than in PREM. (3) At depths between 2000 and 2700 km, the shear velocities are constrained to be only slightly smaller (<0.5%) than in the PREM. Large S^{SV} amplitudes and impulsive S^{SH} waveforms are in excellent agreement with synthetic seismograms computed for M1. The variations in $T_{S^{SH}-SKS}$ are used to estimate shear velocity perturbations in D" and display the presence of short-scale (<500 km) variations, super-imposed on long-scale (>2000 km) trends.

Acknowledgments. We thank Bill Shannon of the Geological Survey of Canada and Harley Benz of the United States Geological Survey for help in assembling CNSN and USNSN broadband data. TERRAscope, BDSN, and IRIS-net broadband data were made available by the data center of the Incorporated Research Institutes of Seismology. We also received waveform data collected by Eric Sandvol and Michael Bostock. Michael Wysession provided codes to compute seismic travel time ellipticity corrections and reprints of papers. Constructive reviews were provided by Donald Helmberger and an anonymous reviewer. S. Thirumalai provided useful comments on earlier drafts of this manuscript. All figures were generated with the GMT software of *Wessel and Smith* [1991]. Parts of this research are funded under NSF grants EAR-9305894 and EAR-9628127 and facilities support to J.R. from the Carnegie Institution of Washington. This is contribution number 316 of the Institute of Tectonics and W. M. Keck Seismological Laboratory.

References

Alexandei, S. S., and R. A. Phinney, A study of the core-mantle boundary using P waves diffracted by Earth's core, *J. Geophys. Res.*, *71*, 5943–5958, 1966.

Chapman, C. H., and R. A. Phinney, Diffracted seismic signals and their numerical solution, *Methods Comput. Phys.*, *12*, 165–230, 1972.

Choy, G. L., Theoretical seismograms of core phases calculated by frequency-dependent full wave theory and their interpretation, *Geophys. J. R. Astron. Soc.*, *51*, 275–312, 1977.

Doornbos, D. J., and J. C. Mondt, *P* and *S* waves diffracted around the core and the velocity structure at the base of the mantle, *Geophys. J. R. Astron. Soc.*, *57*, 381–395, 1979.

Doornbos. D. J., S. Spiliopoulos, and F. D. Stacey, Seismological properties of D" and the structure of a thermal boundary layer, *Phys. Earth Planet. Inter.*, *41*, 225–239, 1986.

Dziewonski, A. M., Mapping the lower-mantle: Determination of lateral heterogeneity in *P* velocity up to degree and order 6, *J. Geophys. Res.*, *89*, 5929–5952, 1984.

Dziewonski, A. M., and D. L. Anderson, Preliminary reference Earth model, *Phys. Earth Planet. Inter.*, *25*, 297–356, 1981.

Dziewonski, A. M., and F. Gilbert, The effect of small, aspherical perturbations on travel times and a re-examination of the corrections for ellipticity, *Geophys. J. R. Astron. Soc.*, *44*, 7–17, 1976.

Fuchs, K., and G. Müller, Computation of synthetics seismograms with the reflectivity method and comparison with observations, *Geophys. J. R. Astron. Soc.*, *23*, 417–4343, 1971.

Garnero, E. J., and D. V. Helmberger, Travel times of *S* and *SKS*: Implications for three-dimensional lower mantle structure beneath the central Pacific, *J. Geophys. Res.*, *98*, 8225–8241, 1993.

Garnero, E. J., and D. V. Helmberger, A very slow basal layer underlying large-scale low-velocity anomalies in the lower mantle beneath the Pacific: Evidence from core phases, *Phys. Earth Planet. Inter.*, *91*, 161–176, 1995a.

Garnero, E. J., and D. V. Helmberger, On seismic resolution of lateral heterogeneity in the earth's outermost core, *Phys. Earth Planet. Inter.*, *88*, 117–130, 1995b.

Garnero, E. J., and D. V. Helmberger, Seismic detection of a thin laterally varying boundary layer at the base of the mantle beneath the central-Pacific, *Geophys. Res. Lett.*, *23*, 977–980, 1996.

Garnero, E. J., D. V. Helmberger, and G. Engen, Lateral variations near the core-mantle boundary, *Geophys. Res. Lett.*, *15*, 609–612, 1988.

Garnero, E. J., D. V. Helmberger, and S. P. Grand, Preliminary evidence for a lower mantle shear wave velocity discontinuity beneath the central Pacific, *Phys. Earth Planet. Inter.*, *79*. 335–347, 1993.

Goes, S., and J. Ritsema, A broadband *P* wave analysis of the large deep Fiji Island and Bolivia earthquakes of 1994, *Geophys. Res. Lett.*, *22*, 2249–2252, 1995.

Hales, A. L., and J. L. Roberts, The velocities in the outer core, *Bull. Seismol. Soc. Am.*, *61*, 1051–1059, 1971.

Helmberger, D. V., E. J. Garnero, and X. Ding, Modeling two-dimensional structure at the core-mantle boundary, *J. Geophys. Res.*, *101*, 13,963–13,972, 1996.

Jeanloz, R., The nature of the Earth's core, *Annu. Rev. Earth Planet. Sci.*, *18*, 357–386, 1990.

Kendall, J.-M., and P. M. Shearer, Lateral variations in D" thickness from long-period shear-wave data, *J. Geophys. Res.*, *99*, 11,575-11,590, 1994.

Kuo, B.-Y., and K.-Y. Wu, Global shear velocity heterogeneities from *Sd-SKS* differential travel times *J. Geophys. Res.*, *102*, 11,775–11,788, 1997.

Lay, T., and D. V. Helmberger, A lower mantle *S* wave triplication and the shear velocity structure of D", *Geophys. J. R. Astron. Soc.*, *75*, 799–838, 1983.

Li, X.-D., and B. Romanowicz, Global mantle shear velocity model developed using nonlinear asymptotic coupling theory, *J. Geophys. Res.*, *101*, 22,245–22,272, 1996.

Liu, X.-F., and A. M. Dziewonski, Lowermost mantle shear wave velocity structure (abstract), *Eos Trans. AGU*, *75*, Fall Meet. Suppl. (44), 663, 1994.

Loper, D. E., and T. Lay, The core-mantle boundary region, *J. Geophys. Res.*, *100*, 6397–6420, 1995.

Masters, G., S. Johnson, G. Laske, and H. Bolton, A shear-velocity of the mantle, *Philos. Trans. R. Soc. London*, *354*, 1385–1411, 1996.

Maupin, V., On the possibility of anisotropy in the D" layer as inferred from the polarization of diffracted *S* waves, *Phys. Earth Planet. Inter.*, *87*, 1–32, 1994.

Mori, J., and D. V. Helmberger, Localized boundary layer below the mid-Pacific velocity anomaly identified from a *PcP* precursor, *J. Geophys. Res.*, *100*, 20,359–20,365, 1995.

Mula, A. H., Amplitudes of diffracted long-period *P* and *S* waves and the velocities and Q structure at the base of the mantle, *J. Geophys. Res.*, *86*, 4999–5011, 1981.

Richter, F. M., Focal mechanisms and seismic energy release of deep and intermediate earthquakes in the Tonga-Kermadec region and their bearing on the depth extent of mantle flow, *J. Geophys. Res.*, *84*, 6783–6795, 1979.

Schweitzer, J., Untersuchung zur Geschwindigkeitsstruktur im unteren erdmantle und im bereich der Kern-Mantelgrenze unterhalb des Pazifiks mit scherwellen, Ph.D. Thesis, Frankfurt Univ., Frankfurt, Germany, 1990.

Stacey, F. D., and D. E. Loper, The thermal boundary layer interpretation of D" and its role as a plume source, *Phys. Earth Planet. Inter.*, *33*, 45–55, 1983.

Stevenson, D. J., Limits on lateral density and velocity variations in the Earth's outer core, *Geophys. J. R. Astron. Soc.*, *88*, 311–319. 1994.

Su, W.-J, R. L. Woodward, and A. M. Dziewonski, Degree 12 model of shear-velocity heterogeneity in the mantle, *J. Geophys. Res.*, *99*, 6945–6980, 1994.

Sylvander, M., and A. Souriau, Mapping S-velocity heterogeneities in the D" region, from SmKS differential times, *Phys. Earth Planet. Inter.*, *94*, 1–21, 1996.

Tanaka, S., and H. Hamaguchi, Degree one heterogeneity at the top of the Earth's core, revealed by SmKS travel times, in *Dynamics of Earth's Deep Interior and Earth Rotation, Geophys. Monogr. Ser.*, vol. 72, edited by J.-L Le Mouël, D. E. Smylie, and T. A. Herring, pp. 127–134, AGU, Washington, D.C., 1993.

Tanimoto, T., Long-wavelength S-wave velocity structure throughout the mantle, *Geophys. J. Int.*, *100*, 327–336, 1990.

Valenzuela, R. W., Lateral and radial velocity structure at the base of the mantle from diffracted shear waves, Ph.D. thesis, 255 pp., Washington University, St. Louis, MO., 1996.

Vinnik, L. V., V. Farra, and B. Romanowicz, Observational evidence for diffracted *SV* in the shadow of the Earth's core, *Geophys. Res. Lett.*, *16*, 519–522, 1989.

Vinnik, L. V., B. Romanowicz, Y. Le Stunff, and L. Makeyeva. Seismic anisotropy of the D" layer, *Geophys. Res. Lett.*, *22*, 1657–1660, 1995.

Williams, Q., and E. J. Garnero, Seismic evidence for partial melt at the base of Earth's mantle, *Science*, *273*, 1528–1530. 1996.

Wessel, P., and W. H. F. Smith, Free software helps map and display data, *Eos Trans. AGU*, *72*, 441, 445–446, 1991.

Wysession, M. E., Continents of the core, *Nature*, *381*, 373–374, 1996.

Wysession, M. E., E. A. Okal, and C. R. Bina, The structure of the core-mantle boundary from diffracted waves, *J. Geophys. Res.*, *97*, 8749–8764, 1992.

Wysession, M. E., R. W. Valenzuela, A.-N Zhu, and L. Bartkó, Investigating the base of the mantle using differential travel times, *Phys. Earth Planet. Inter.*, *92*, 67–84, 1995.

Young, C. J., and T. Lay, The core shadow zone boundary and lateral variations of the P velocity structure of the lowermost mantle, *Phys. Earth Planet. Inter.*, *54*, 64–81, 1989.

Young, C. J., and T. Lay, Multi-phase analysis of the shear velocity structure in the D" region beneath Alaska, *J. Geophys. Res.*, *95*, 17,385–17,402, 1990.

E. Garnero and T. Lay, Institute of Tectonics, University of California, Santa Cruz, CA 95064. (e-mail: eddie@earthsci.ucsc.edu; thorne@earthsci.ucsc.edu)

J. Ritsema, Department of Geological Sciences, University of South Carolina, Columbia, SC 29208. (e-mail: jeroen@seis.sc edu)

(Received February 19, 1997; revised May 9, 1997; accepted May 16, 1997.)